Evidence of multiferroicity in NdMn$_2$O$_5$

S. Chattopadhyay,[1,*] V. Balédent,[1] F. Damay,[2] A. Gukasov,[2] E. Moshopoulou,[3] P. Auban-Senzier,[1] C. Pasquier,[1] G. André,[2] F. Porcher,[2] E. Elkaim,[4] C. Doubrovsky,[1] M. Greenblatt,[5] and P. Foury-Leylekian[1]

[1]*Laboratoire de Physique des Solides, CNRS, Univ. Paris-Sud, Université Paris-Saclay, 91405 Orsay Cedex, France*
[2]*Laboratoire Léon Brillouin, CEA-CNRS, UMR12, 91191 Gif-sur-Yvette Cedex, France*
[3]*Institute of Materials Science Demokritos, National Center for Scientific Research, 15310 Agia Paraskevi, Athens, Greece*
[4]*Soleil Synchrotron, 91191 Gif-sur-Yvette Cedex, France*
[5]*Department of Chemistry and Chemical Biology, Rutgers, the State University of New Jersey, Piscataway, New Jersey 08854, USA*

Recently, RMn$_2$O$_5$ (R = rare earth, Bi, Y) type multiferroics have drawn considerable attention, because of magnetically induced ferroelectricity along with an extremely large magnetoelectric coupling. Here, we present a detailed study on NdMn$_2$O$_5$ which is a crucial composition between the nonferroelectric PrMn$_2$O$_5$ and ferroelectric SmMn$_2$O$_5$. We report the results of heat capacity, magnetization, dielectric permittivity, and electric polarization measurements along with an accurate description of the structural and microscopic magnetic properties obtained from high resolution x-ray and neutron diffraction studies. We show that NdMn$_2$O$_5$ is ferroelectric, although the magnitude of polarization is much weaker than that of the other multiferroic members. The direction of the polarization is along the crystallographic b axis and its magnitude can be tuned with the application of a magnetic field. Moreover, unlike the other multiferroic members of this series, ferroelectricity in NdMn$_2$O$_5$ emerges in an incommensurate magnetic state. The present study also provides evidence in support of the influence of the rare-earth size on the magnetoelectric phase diagram.

I. INTRODUCTION

Magnetoelectric multiferroic compounds, characterized by the simultaneous presence of magnetic and electric ferroic/antiferroic coupled orders, are exceptional multifunctional materials opening a new horizon for next generation electronic devices. They respond to both applied electric and magnetic fields and thus can provide a much better degree of control than systems with only one ferroic order (ferro/antiferromagnetism or ferroelectricity) [1]. However, the actual challenge in the field of such multiferroics is to maximize the cross coupling between ferroelectricity and magnetism. Very strong cross coupling is expected in a system, when the ferroelectricity is magnetically induced. This type of spin-induced ferroelectricity is commonly observed in materials with complex magnetic orders generally arising from magnetic frustration. The microscopic mechanism, usually proposed to account for such spin-induced ferroelectricity, is the antisymmetric Dzyaloshinskii-Moriya (DM) interaction between noncollinearly ordered spins, which favors the displacement of negatively charged ligands that induces electric polarization in the system by breaking the inversion symmetry [2,3].

Recently, a different kind of spin-induced ferroelectricity has been observed in the magnetically frustrated RMn$_2$O$_5$ (R = lanthanide, Bi, Y) family of oxides. In this series, ferroelectricity has been found to be induced by nearly collinear magnetic ordering. Thus, the origin cannot be explained by the standard DM model. The mean structure of the RMn$_2$O$_5$ compounds crystallizes in the centrosymmetric orthorhombic *Pbam* space group [4,5]. However, a slight deviation from the mean structure has been recently detected in single crystals

for all the members of the series [6]. In the mean structure, there are two distinct crystallographic sites for Mn^{4+} (site $4f$) and Mn^{3+} (site $4h$) forming Mn^{3+}O$_5$ square pyramids and corner sharing Mn^{4+}O$_6$ octahedra (see Fig. 1). In the (a,b) plane, loops of five Mn ions (three Mn^{3+} and two Mn^{4+}) are formed. In each loop, three inequivalent nearest-neighbor antiferromagnetic (AF) superexchange interactions are present between Mn ions (see Fig. 1): J_3 and J_4 between Mn^{3+} and Mn^{4+} spins, and J_5 between two Mn^{3+} spins which is also expected to be the dominant integral [7]. Since all of them are AF, this induces a magnetic frustration in the system [3]. Along the c direction, Mn^{4+}O$_6$ octahedra share edges to form ribbons (see Fig. 1). In between two adjacent layers of Mn^{4+} ions, layers of Mn^{3+} and R^{3+} appear alternatively. Due to such a specific kind of atomic arrangement, two types of Mn^{4+}-Mn^{4+} exchange interactions, viz., J_2 (through the Mn^{3+} layers) and J_1 (through the R^{3+} layers) [Fig. 1(b)] become relevant along c. The main contribution to J_2 is the Mn^{4+}-Mn^{3+} superexchange coupling and it is always ferromagnetic (F) [7,8].

The members of the series with small R^{3+} ions (from Tb to Lu) have been intensively studied and ferroelectricity has been evidenced in all of them. Moreover, an extremely large and reversible magnetoelectric coupling has been observed in TbMn$_2$O$_5$ [9–11]. These multiferroic members of the RMn$_2$O$_5$ series are well known for showing multiple phase transitions. In these compositions, the first magnetic transition (ICM1 at $T_{C1} \approx 42$–45 K) is generally associated with an incommensurate propagation vector $q_M = (0.5 - \delta, 0, \tau)$ ($\delta \approx 0.01$ and $0.25 \leqslant \tau \leqslant 0.35$) and a quasicollinear spin arrangement. Below $T_{C2} \approx 38$–41 K, the propagation vector of the magnetic order becomes commensurate (CM) with $q_M = (0.5,0,0.25)$ and an electric polarization concurrently sets in generally along the b axis [3]. Near $T_{C3} \approx 20$–25 K, the magnetic propagation vector recovers its incommensurate character (ICM2) and

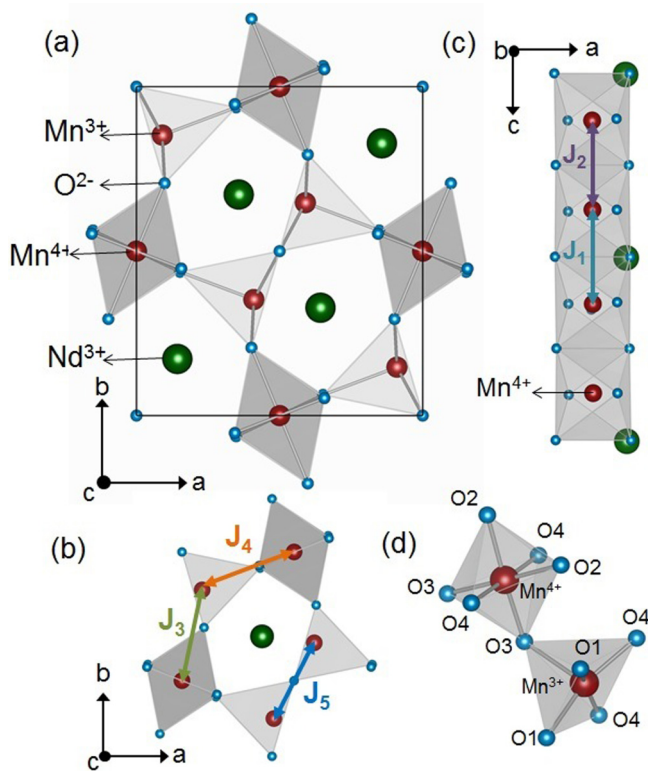*Corresponding author: ch.sumanta@gmail.com

FIG. 1. (a) A perspective view of the crystal structure of RMn$_2$O$_5$. Magnetic exchange interactions (J_i) (b) in the (a,b) plane and (c) along the c direction. (d) A magnified representation of Mn^{4+}O$_6$ octahedron and Mn^{3+}O$_5$ square pyramid.

finally the R^{3+} spins generally undergo a magnetic ordering below 10 K.

As mentioned, the spin-induced ferroelectricity, observed in these materials with nearly collinear spin alignments, cannot be described by the standard DM model suitable for noncollinear magnetic orderings. Instead, an *exchange-striction* based mechanism is proposed to explain the origin of ferroelectricity in this series. It is argued that due to the exchange-striction effect, all the Mn^{3+} ions slightly move from their centrosymmetric positions to release the magnetic frustration. In this way, the inversion symmetry is broken (in particular, the a glide plane symmetry), which induces the ferroelectricity along the b direction [3,8,9]. This polarization is expected to be proportional to the scalar product of the adjacent Mn spins and thus it becomes strong when the magnetic structure is collinear. In this multiferroic series, the magnetic structure is strongly influenced by the nature of the R^{3+} ions and the magnitude of the ferroelectric (FE) polarization strongly depends on the exact magnetic structure. For instance, in DyMn$_2$O$_5$ the spins lie along the b axis in the phase of highest electric polarization, while for the other compounds of the series the magnetic easy axis is mostly along the a direction. A key issue is thus to understand the influence of the rare earth on the magnetic ordering or, more generally, on the magnetoelectric properties of the system. However, to acquire in-depth understanding of this issue, detailed investigations on the compositions with large R^{3+} ions ($R = $ Pr, Nd, Sm) are essential. Due to the

synthesis difficulties, the possible multiferroic properties of these compounds have yet to be studied. Fortunately, we have recently succeeded in synthesizing high quality powders and small single crystals of such compositions.

We have already reported our results on PrMn$_2$O$_5$ and have shown that this compound strongly differs from the members with small R^{3+}. It has been observed that PrMn$_2$O$_5$ is paraelectric and undergoes two commensurate magnetic transitions at 25 and 20 K [12,13]. On the other hand, SmMn$_2$O$_5$ is known to be FE. With this scenario, the composition NdMn$_2$O$_5$ can be regarded as a threshold case as it lies in between paraelectric PrMn$_2$O$_5$ and ferroelectric SmMn$_2$O$_5$. Therefore, an investigation of this composition is essential to understand the series in a better way. It is to be noted that the issue of multiferroicity in NdMn$_2$O$_5$ will be well addressed here. Moreover, regarding the magnetism of the system, only the ground state magnetic structure has been determined [14] but by using low resolution powder neutron diffraction data. Recently, the magnetic phase diagram has been investigated [15,16] with a determination of the magnetic propagation wave vector in the different phases. However, the magnetic structure in the different magnetic phases is still missing. In this work, we have thus studied not only the multiferroic behaviors, but we have also revisited the magnetic structure of this composition in the ferroelectric state with a high resolution neutron spectrometer and taking into consideration the recent results obtained for the magnetic structures of the other members of the series [9].

II. SYNTHESIS AND ROOM TEMPERATURE STRUCTURAL CHARACTERIZATION

Polycrystalline NdMn$_2$O$_5$ was synthesized following the methodology as described in Refs. [12,16]. Single crystals were synthesized following the method of Ref. [17]. Highly pure Na$_2$MoO$_4$, MoO$_3$, MnCO$_3$, and Nd$_2$O$_3$ were mixed in a molar ratio of 3.5 : 1.5 : 0.5 : 0.6. This mixture was electrolyzed for 16 h at 990 °C using platinum electrodes and an Al$_2$O$_3$ crucible. The as-grown crystals were finally washed with warm solutions of 5% K$_2$CO$_3$ and 2.5% disodium ethylenediaminetetraacetate. The black and shining single crystals obtained from this synthesis have two kinds of morphology. Most of the crystals are platelike (0.5 mm^2), similar to PrMn$_2$O$_5$. However, few of them have a needlelike shape (0.1 mm^2), similar to TbMn$_2$O$_5$ crystals and the crystals obtained by Euzen *et al.* [18]. We have characterized both of these two types of crystals.

A high resolution powder x-ray measurement was performed with synchrotron radiation on the high purity NdMn$_2$O$_5$ powder. The measurement was carried out at the CRISTAL beamline of the Soleil synchrotron light source in France. The x-ray wavelength used was 0.62 Å. The experiment was carried out between $2\theta = 0°$ and $50°$ at 300 K. Rietveld refinement of the integrated intensities was performed using the GSAS software package [19]. It is in good agreement with the 300 K crystallographic structure and the *Pbam* centrosymmetric space group reported previously [4,5] (see Table I). In addition, we did not observe any impurity phase in this sample.

TABLE I. Atomic positions and unit cell parameters (Å) of the powder, needlelike, and platelike samples obtained from the x-ray scattering experiment at 300 K.

	a	b	c
Powder	7.5123(1)	8.6236(2)	5.7045(1)
Atom	x	y	z
Nd	0.1429(1)	0.1730(1)	0
Mn^{4+}	0	0.5	0.2592(1)
Mn^{3+}	0.4100(2)	0.3514(1)	0.5
O1	0	0	0.2773(1)
O2	0.1602(5)	0.4530(5)	0
O3	0.1518(50)	0.4359(37)	0.5
O4	0.4001(3)	0.2047(3)	0.2488(4)
	a	b	c
Needle	7.4146	8.5776	5.6784
Atom	x	y	z
Nd	0.141 71(1)	0.172 60(2)	0
Mn^{4+}	0	0.5	0.257 41(3)
Mn^{3+}	0.409 82(1)	0.351 57(1)	0.5
O1	0	0	0.275 40(2)
O2	0.158 35(6)	0.447 17(7)	0
O3	0.152 32(15)	0.434 69(17)	0.5
O4	0.400 09(6)	0.207 26(7)	0.247 04(6)
	a	b	c
Plate	7.4907	8.622	5.7010
Atom	x	y	z
Nd	0.142 23(2)	0.172 65(2)	0
Mn^{4+}	0	0.5	0.258 16(3)
Mn^{3+}	0.410 10(1)	0.352 10(2)	0.5
O1	0	0	0.277 27(5)
O2	0.157 59(7)	0.447 964(5)	0
O3	0.153 51(12)	0.436 23(18)	0.5
O4	0.402 23(9)	0.206 385(8)	0.2503 28(9)

We carried out structural measurements on the two types of single crystals in a laboratory based four-circle diffractometer working with a Mo $K\alpha$ wavelength. The structural refinement was performed with SHELX software [20]. The results obtained from the refinement are given in Table I. We can notice that the unit cell parameter along the a direction is much smaller ($\sim 10^{-1}$ Å) for the needlelike crystals than that of the platelike and powder samples (see Table I). This value of a also differs from the value reported earlier in the literature [5]. In addition, we have observed that in the case of the needles, the Mn^{3+}-O3 distance [see Fig. 1(d)] is always shorter (2.0720, 2.0544, and 2.0380 Å for the powder, platelike, and needlelike samples, respectively). This may lead to an enhanced J_4 exchange interaction. Thus, the structural anomalies of the needlelike crystal should have a strong influence on its magnetic orderings and also on other physical properties.

We have checked the stoichiometry and chemical purity of the various samples using an energy dispersive x-ray spectroscopy technique (EDS) and x-ray diffraction. The oxygen stoichiometry has been checked via the refinement of the x-ray data. The refinements for all the samples have shown a roughly nominal oxygen stoichiometry (the sensitivity of x rays to oxygen cannot give very accurate values). From EDS measurements, we have observed that the single crystals

present a small amount of nonmagnetic Al contamination (a few atomic percent) probably due to the alumina crucible used at high temperature during the electrolysis. The Al contaminant does not form any aggregate because no impurity has been detected as a second phase in the x-ray measurements. It rather forms a solid solution mainly at the surface of the crystals. The Nd:Mn molar ratio has been found to be as per the chemical formula unit for both powder and platelike single crystals. However, the EDS analysis shows that the needlelike single crystals have a strong Nd deficiency (66 at. % for Mn and 28 at. % for Nd). If the oxygen is stoichiometric, this Nd deficiency must be compensated by the presence of excess Mn^{3+} replacing some Mn^{4+} ions to maintain the electroneutrality. This could be the possible reason for the anomalous unit cell parameter observed in the needlelike crystal.

III. RESULTS

A. Calorimetric and bulk magnetic properties

Heat capacity (C_p) measurements were performed on the two types of single crystals with a physical property measurement system (PPMS) from Quantum Design. For each type of sample, the reproducibility of the data was verified by repeated measurements. The results are presented in Fig. 2. $C_p(T)$ measurements performed on the platelike single crystal produce similar behavior as the powder sample published in Ref. [16], but with a shift of the high temperature anomaly. A broad peak can be seen around $T_{1SC} = 25 \pm 2$ K in the C_p/T vs T data. With cooling, another weak anomaly at $T_{3SC} = 17 \pm 2$ K is observed. When the temperature is decreased further, a sharp feature appears around $T_{4SC} = 4 \pm 1$ K. As reported recently [16], the powder sample shows four anomalies at $T_{1P} = 30 \pm 2$ K, $T_{2P} = 26 \pm 2$ K, $T_{3P} = 17 \pm 2$ K, and $T_{4P} = 4 \pm 2$ K.

In comparison, heat capacity data of the needle-shaped crystals show only one transition at $T_{4N} = 5 \pm 1$ K, as depicted in the inset of Fig. 2. This strong difference is certainly related
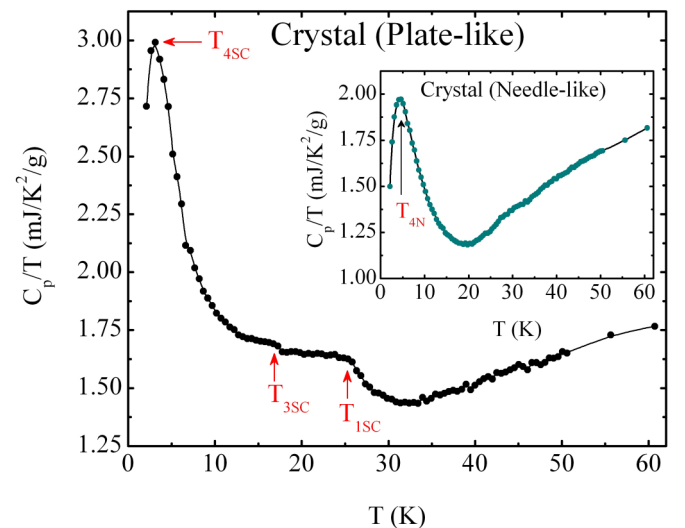

FIG. 2. Thermal variation of the heat capacity (C_p) over temperature (T) for the platelike and (inset) needlelike crystals.

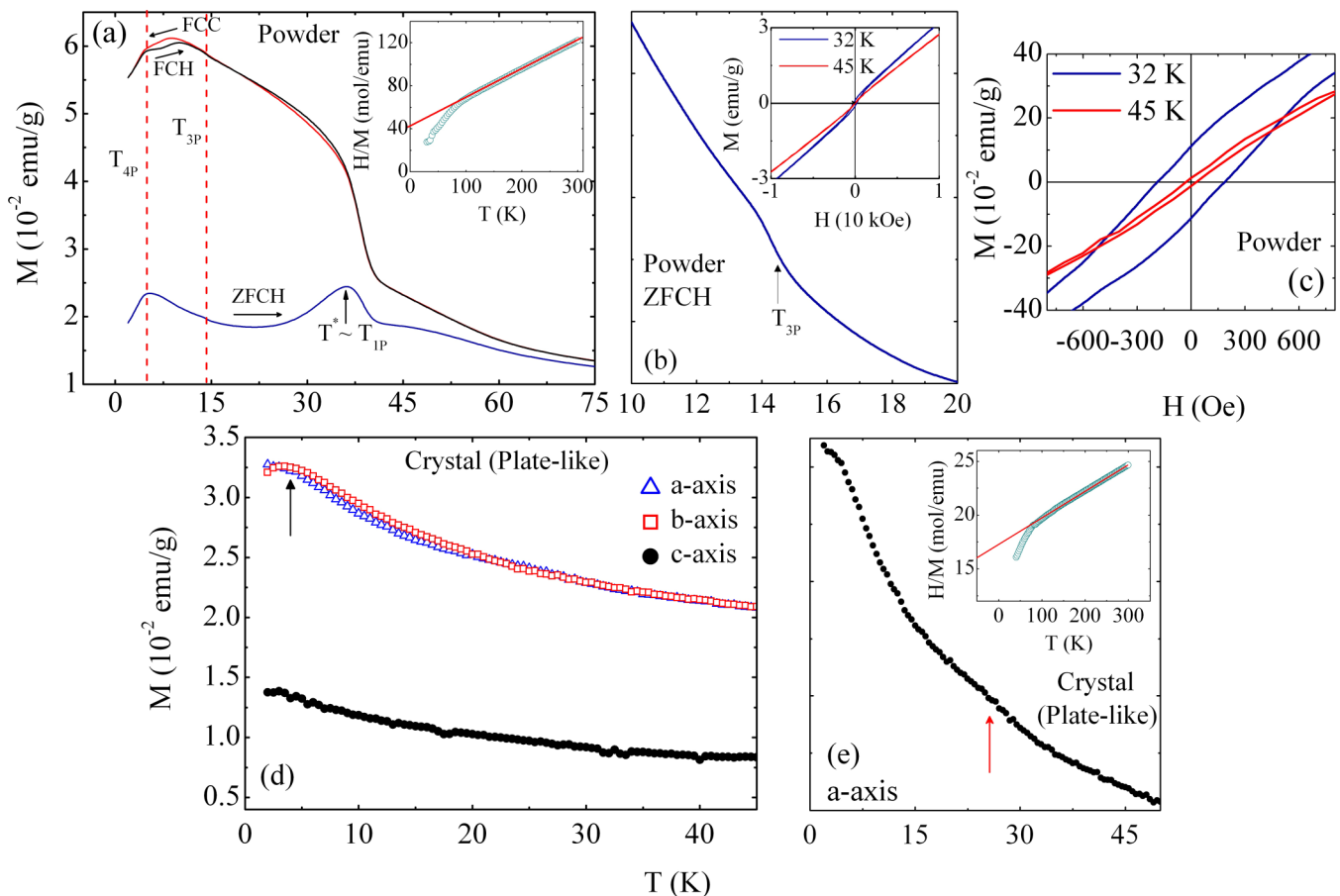FIG. 3. (a) Temperature (T) dependence of magnetization (M) for the powder sample measured in zero field cooled heating (ZFCH), field cooled cooling (FCC), and field cooled heating (FCH) protocols with an applied magnetic field of 100 Oe. Inset: Curie-Weiss fitting of the inverse susceptibility data as a function of temperature. (b) ZFCH $M(T)$ data of the powder sample emphasizing the anomaly at T_{3P}. Inset: $M(H)$ curves measured at 32 and 45 K. (c) Low field region of the $M(H)$ curves to show the hysteresis effect. (d) Zero field cooled $M(T)$ data of the platelike crystal measured along three different crystallographic axes with a field of 1 kOe. (e) $M(T)$ data along the a direction for the same type of crystal emphasizing the magnetic transition. Inset: Curie-Weiss fitting of the inverse susceptibility data as a function of temperature.

to the structural dissimilarities among the needle-shaped crystal and the other samples. Such significant discrepancies, as observed in the structural parameters as well as in the heat capacity data, lead us to focus only on the platelike crystals and the powder samples for the rest of our study. It is to be noted that for the powder and the platelike samples, the overall behavior of the heat capacity data, including the multiple phase transitions, is very similar to other multiferroic members of the RMn$_2$O$_5$ series [21].

In order to verify whether the phase transitions observed in the heat capacity measurements have magnetic origins, we performed magnetization (M) measurements with a commercial superconducting quantum interference device (SQUID) magnetometer (Quantum Design). The magnetization data are found to be in line with the heat capacity result. As reported recently by us [16], the zero field cooled heating (ZFCH) data of the powder sample measured under a magnetic field (H) of 100 Oe [Fig. 3(a)] show an anomaly around $T^* = 36 \pm 2$ K, which is close to T_{1P}. This feature is followed by two other anomalies near 15 ± 1 K ($\sim T_{3P}$) and 4 ± 1 K (T_{4P}). From the Curie-Weiss type fitting of the ZFCH data above 120 K, we found the Curie-Weiss temperature (θ) to be -161 K,

signifying the presence of AF correlations in the system. The ratio $|\theta/T_{1P}|$ turned out to be 5.4, reflecting that this system is moderately frustrated [22]. The thermomagnetic irreversibility that appears below 120 K between the ZFC and the field cooled curves [16] is presumably related to a small ferromagnetic component present in the system, since we have observed a hysteresis loop in the low magnetic field regime of the $M(H)$ data measured at 45 and 32 K (Fig. 3). The origin of this small ferromagnetic component is possibly related to the canting of the spins. As will be discussed later, the magnetic structure at low temperature shows the presence of highly noncollinear spin orientations. So, it is likely that this low field hysteresis could be connected to the onset of a short range magnetic correlation with spin canting even well above the true magnetic ordering. Such short range orderings are often observed in the magnetically frustrated systems well above long range ordering. From the field cooled cooling (FCC) and field cooled heating (FCH) curves, one can observe the presence of two thermal hysteresis spanning over $\delta T \approx 10$ K. The first one appears below T^* and includes the T_{2P} transition, whereas the second hysteresis is present around the T_{4P} transition. This result is an indication of the first-order character of

the corresponding phase transitions. Such multiple thermal hysteresis has also been observed in $DyMn_2O_5$ [23].

Magnetization measurements were also performed on the platelike single crystal following the ZFCH protocol. Figure 3(d) depicts the thermal variation of M along three different crystallographic axes between 2 and 45 K. In the entire temperature range, the magnetization measured along c is much smaller than the one measured along the remaining two directions. There is practically no anisotropy present between the a and b directions. Thus, the easy plane for the spins should be the (a,b) plane. In addition, the high temperature magnetic phase transition is also evidenced by this single-crystal measurement. It is characterized by a weak anomaly near 26 ± 1 K ($\sim T_{1SC}$) in the $M(T)$ curve measured along the a direction [Fig. 3(e)]. This feature seems to signify that the spins related to this ordering have components mostly along a. A closer look at the $M(T)$ data along b reveals a humplike feature [indicated with an arrow in Fig. 3(d)] with its maximum at T_{4SC}. This is a possible signature of the AF character of the low temperature phase transition similar to many other compositions from this series. The fact that the transition at T_{4SC} is only visible along b indicates that the b components of the spins are predominantly involved in this transition.

For the crystal, the $|\theta/T_{1SC}|$ ratio turns out to be ~ 9.2, where the θ value was estimated from the Curie-Weiss fitting of the high temperature susceptibility data along the c direction. Clearly, the magnetic frustration is much weaker in the powder than in the crystal. Such a reduction in the strength of the frustration is related to the enhancement of the surface over volume ratio in the powder sample. Similar behavior has also been observed previously in strongly frustrated $ZnCr_2O_4$ [24]. The role of magnetic frustration is to prevent the long range magnetic ordering. Therefore, in the platelike crystal, the lowering of the magnetic ordering temperature as compared to the powder sample is possibly related to this enhanced magnetic frustration. Moreover, the surface impurities can also have some role in this issue.

B. Electric properties

The temperature dependence of the complex dielectric permittivity (ϵ) was measured between 40 and 10 K with varied frequencies using an RLC bridge (HIOKI 5322) and a laboratory-made shielded sample holder. Experiments were performed both on a pellet and a single crystal. For the single-crystal experiment, the signal-to-noise ratio was improved by averaging the measurements and by slowing down the temperature sweep rate in order to have both ϵ' and ϵ''. However, their absolute values are not known very precisely as the contribution of the cables (of the order of 1 pF for the capacitance) and their frequency dependence were difficult to evaluate. The thermal dependence of ϵ' measured on a pellet of $NdMn_2O_5$ powder [Fig. 4(a)] shows a peak around 26 ± 2 K, a temperature very close to T_{2P}. Since, there is practically no frequency dependence on the peak position and as it also looks similar to the one observed in other FE members of RMn_2O_5, this peak could be a fingerprint of a ferroelectric transition. It is important to mention that the first-order nature of the ferroelectriclike transition (similar to the other FE

members) was confirmed by performing the heating-cooling thermal cycle measurement of $\epsilon'(T)$. As depicted in the inset of Fig. 4(a), a prominent thermal hysteresis is present in the $\epsilon'(T)$ data. This feature is also in line with the high temperature thermal hysteresis observed in the $M(T)$ data. Near T_{3P}, the $\epsilon'(T)$ curve shows a weak anomaly. The possible origin of this anomaly, in connection with the famous electromagnon excitation, is discussed in Ref. [16]. In Fig. 4(b), the $\epsilon'(T)$ measurement performed on one platelike single crystal along the b axis is presented for three different frequencies. These curves show a very similar behavior as for the powder sample, which indicates that the electric polarization is mostly along the b direction as in the other FE members of the series. For crystals, the peak in the $\epsilon'(T)$ curve is observed around $T_{2SC} = 20 \pm 2$ K, a temperature shifted by about 5 K with respect to the T_{2P} transition of powders. For the single crystal, the thermal evolution of the dielectric loss $\epsilon''(T)$ [inset of Fig. 4(b)] confirms the presence of an anomaly at the same temperature as for $\epsilon'(T)$. All these results indicate that the second transition has an impact on the electric properties.

In order to have direct evidence of the ferroelectriclike transition observed in $\epsilon'(T)$, a pyroelectric current (I_{pyro}) measurement was carried out as a function of T. The sample was initially cooled down to 10 K under a constant poling electric field (E_{pole}) (delivered by a Keithley 6487 picoammeter/voltage source). After cooling, the poling field was switched off and the sample electrodes were short circuited for 1 h to maintain the zero charge condition. Then the sample was warmed at a rate of 5 K/min to measure the temperature variation of I_{pyro} with the picoammeter [Fig. 4(c)]. The electric polarization (P) was estimated as a function of temperature by integrating this I_{pyro} data. During the first measurement performed on a pellet of the powder sample, a weak peak in the $I_{pyro}(T)$ was observed around T_{2P}. This feature became stronger with increasing E_{pole} and finally the magnitude of I_{pyro} got saturated for $E_{pole} = 7$ kV cm^{-1}. By applying $E_{pole} = -7$ kV cm^{-1}, we observed exactly the same behavior of $I_{pyro}(T)$ but with a reversed sign. The temperature variation of P, as estimated by integrating $I_{pyro}(T)$ for $E_{pole} = 7$ kV cm^{-1}, is depicted in Fig. 4(e). It confirms that below T_{2P}, a spontaneous electric polarization sets in and it increases sharply to reach a maximum value of 0.3 μC/m^2 at 20 ± 1 K. Interestingly, the polarization decreases sharply below 20 K and finally changes its sign with further lowering of temperature. A pyroelectric current measurement following the same protocol was performed on the platelike crystals as well [Fig. 4(d)]. Due to the small size of these crystals, we used a combination of six coaligned crystals to enhance the signal. Each of the crystals used had a thickness of ~ 200 μm. This coalignment helped to obtain a total surface area of ~ 3 mm^2. We applied a poling electric field of 18 kV cm^{-1} along the b direction. This value of E_{pole} is well above the magnitude required to saturate I_{pyro} (here, I_{pyro} saturates for $E_{pole} = 15$ kV cm^{-1}). Figure 4(f) represents the thermal variation of the electric polarization. The behavior is very similar to the one observed in the powder sample. However, the maximum value of polarization is ~ 10 times larger in the crystal. In addition, the critical temperature of the FE phase (T_{SC2}) is decreased by ~ 7 K in the crystal. We also measured the thermal variation of P in the presence of magnetic field
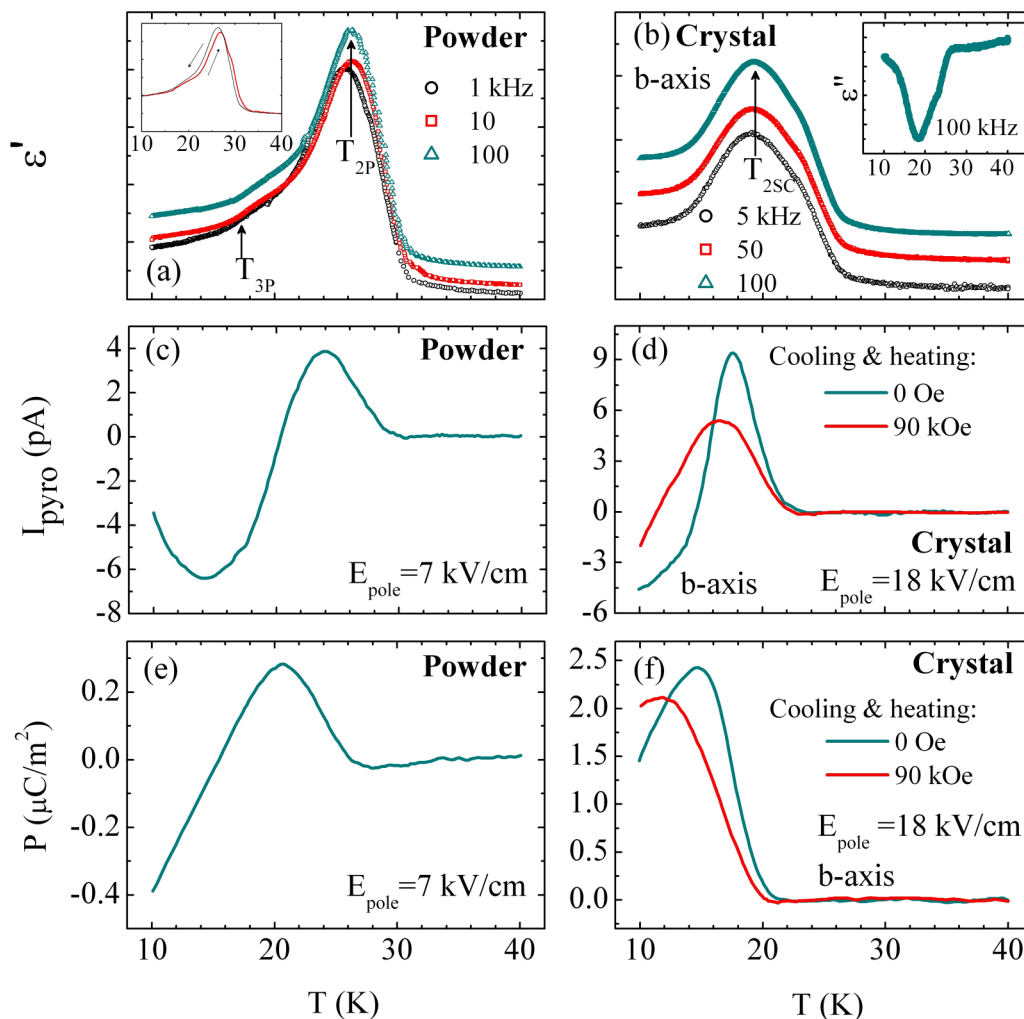
FIG. 4. Temperature dependence of the real part of dielectric permittivity (ϵ') for both (a) powder and (b) platelike crystal (along b). The inset of (a) shows the presence of thermal hysteresis in ϵ' of the powder sample. The thermal variation of the imaginary part of the dielectric permittivity (ϵ'') for the platelike crystal measured at 100 kHz along the b axis is depicted in the inset of (b). The background is unknown and has not been subtracted from the measured dielectric data. Thermal variations of the pyroelectric current are shown for the (c) powder and (d) platelike crystal (along b). For the crystal, data have been shown for measurements performed in zero magnetic field as well as with a field of 90 kOe. Electric polarization (P) of the powder sample as a function of T measured in zero magnetic field is shown in (e), whereas (f) depicts the temperature variation of P along the b direction for the platelike crystal measured in zero magnetic field as well as with a field of 90 kOe.

in order to verify the existence of magnetoelectric effect [Fig. 4(f)]. By applying a field of 90 kOe along the b axis, one can have a $\sim$12% decrease on the maximum of P along with a shift of the peak position towards the lower temperature. Such an effect is also observed in other compounds of the series such as $DyMn_2O_5$ [25,26] and could be due to the progressive suppression of the AF-like magnetic order under magnetic field which induces the electric polarization.

From these measurements, it can be argued that similar to the other members of the series with small R^{3+} size and in contrast with the members with large R^{3+} size (Pr and La), $NdMn_2O_5$ is FE below T_{2P} (or T_{2SC} for crystal). We can also see that the direction of the polarization is along b, as expected. On the other hand, the thermal variation of the electric polarization is not very typical. The sudden decrease of P below 20 K (for the crystal it is 16 K) is the fingerprint of a more complex phase. However, this type of behavior is not unusual in the RMn_2O_5 series and a similar feature has been

observed in compositions with $R =$ Tb and Dy. It can be either due to the variation of the magnetic structure with T which induces a thermal variation of the spin-induced polarization [3], or due to the presence of multiple electric sublattices similar to $DyMn_2O_5$ producing a ferrielectric state [26]. In the case of $NdMn_2O_5$, we can interpret that this unusual thermal behavior results from a complex variation of the magnetic structure, as will be discussed later (Fig. 6).

C. Thermal evolution of the crystal structure

Between 3 and 50 K, we performed the same high resolution powder x-ray measurement as that at 300 K using an identical wavelength of the synchrotron radiation. The Rietveld refinement of the 50 K diffractogram using FULLPROF software [27] is in agreement with the 300 K crystallographic structure. Even at 3 K, we did not observe any significant variation of the intensity of the Bragg reflections. No additional reflections
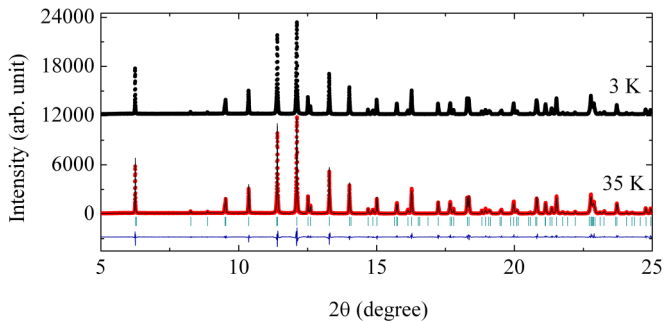
FIG. 5. Powder x-ray diffraction patterns recorded at 35 K (represented along with Rietveld refinement) and 3 K using synchrotron based radiation at the CRISTAL beam line (Soleil, France).

were detected (Fig. 5) as well. In the limit of our x-ray powder diffraction sensitivity ($\sim10^{-2}$ of the intensity of the mean Bragg reflections), this result signifies that the successive transitions of $NdMn_2O_5$ do not directly involve the lattice. Rather, they presumably have a magnetic origin without a significant exchange-striction effect. With the platelike crystal also, we did not find any signature of an exchange-striction effect below T_{2SC}, even after achieving a noise over mean Bragg intensity ratio of $\sim10^{-4}$ in a laboratory based three-circle diffractometer. An accurate refinement of the powder diffractograms is difficult, due to the strong asymmetry in the profiles of the reflections. Such asymmetry is attributed to the grain size and the strain effects, which gets emphasized by the high resolution of the synchrotron beam.

D. Thermal evolution of the magnetic order

To investigate the magnetic properties of $NdMn_2O_5$ with microscopic detail, a neutron powder diffraction (NPD) measurement was carried out in the $G4_1$ diffractometer installed on the cold source at the Orphée-LLB reactor (France). The measurement was performed using the same powder sample
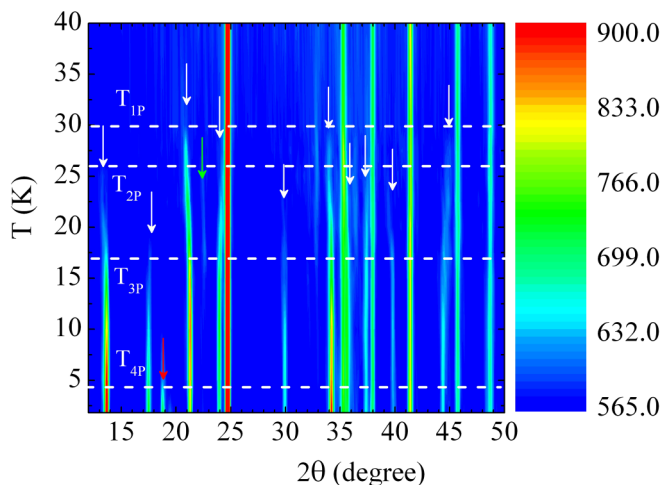

FIG. 6. Color mapping of the NPD patterns collected between 30 and 2 K. The white, red, and green arrows indicate the magnetic reflections corresponding to q_1 (also q_2), q_{CM}, and $3q_1$ propagation vectors, respectively.

with a neutron wavelength of 2.42 Å in order to improve the low angle accuracy. The diffractograms were recorded for $2\theta = 6°$–$86°$ in the temperature range between 2 and 30 K with an increment of 2.5 K. The Rietveld refinement, performed on the 30 K data with the FULLPROF software, is in agreement with the x-ray results. It shows that the structure at 30 K is similar to the one at room temperature.

Below $T_{1P} = 30$ K, a set of around seven new reflections can be detected (Fig. 6). The magnetic origin of these reflections is obvious since no additional reflections have been detected in the x-ray measurement at this temperature. The width of these reflections (except two of them at low angle) is found to be similar to those of the nuclear reflections. This is a prominent signature of long range magnetic order. These reflections can be indexed with an incommensurate propagation vector of the type $q_1 = (\frac{1}{2},0,0.4-\delta)$ with δ decreasing with decreasing temperature. The components of this propagation wave vector are similar to the ones found in the other compositions of the RMn_2O_5 series. However, the c^* component is slightly larger than what is generally observed in these compounds. It is interesting to notice that a very weak reflection, which can be indexed with $3q_1$, can also be seen. This might be a fingerprint of the presence of *higher harmonics of the spin modulation* associated with the magnetic ordering. The presence of such higher harmonics of the spin modulation has already been observed in $TbMn_2O_5$ [28].

Interestingly two reflections, viz., $(0.5,0,0.4-\delta)$ and $(0.5,1,0.4-\delta)$, present in the low angle region of our measurement, are very broad and cannot be well indexed with a unique propagation wave vector. Recent works on the $NdMn_2O_5$ system [15,16] have proposed the possibility of the presence of two slightly different propagation wave vectors. The two propagation wave vectors (we will be denoting them as q_1 and q_2 following the convention of Ref. [16]) have the same a^* component $(0.5a^*)$ but they slightly differ in their c^* components (close to $0.4c^*$). The c^* component of q_1 evolves with temperature similarly to some other RMn_2O_5 compounds [29,30] while q_2 is nearly constant with temperature. Finally, at 15 K (i.e., near T_{3P}), the two magnetic propagation wave vectors merge together with a c^* component very close to 0.4. The magnetic phase between 30 K (T_{1P}) and 15 K ($\sim T_{3P}$) will be denoted as ICM1.

To verify the presence of two different propagation wave vectors in the ICM1 phase, we also performed neutron diffraction measurements with one of the platelike single crystals, in spite of its very small size. This experiment confirms the presence of two propagation wave vectors with slightly different c^* components [see Fig. 7(a)]. These c^* components are slightly greater than $0.4c^*$ and thus are slightly different than the ones observed in the powder sample and reported in Ref. [15]. This very slight discrepancy is however considered to be insignificant compared to the main common features observed, such as the presence of a double q and its incommensurate character in the entire range of temperature. Our measurement also indicates a slight broadening of the a^* component. This feature can be attributed either to a short range magnetic order or to the splitting of the reflection due to a slightly incommensurate character of the propagation vectors along the a^* direction. The stabilization of a magnetic order characterized by two nearly equal propagation wave vectors is
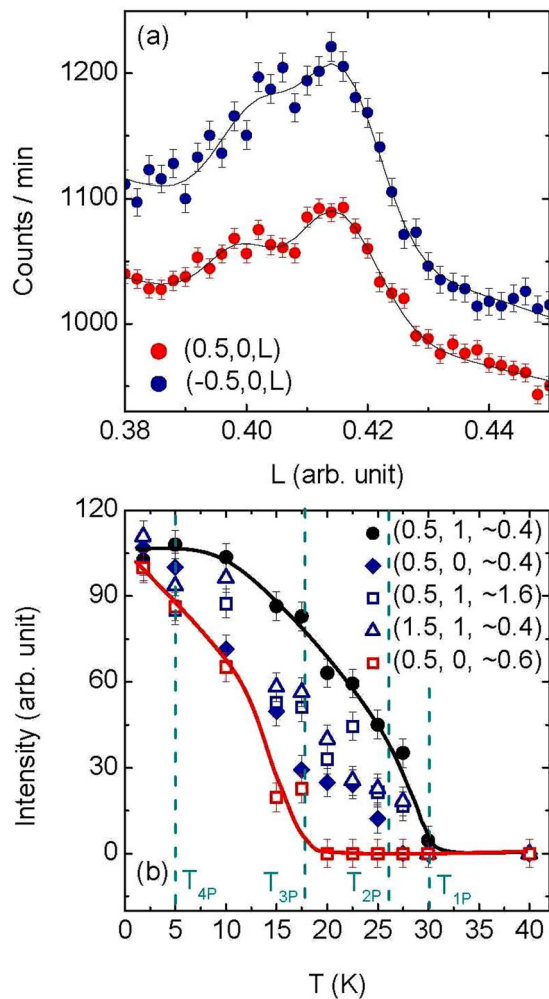
FIG. 7. (a) Single-crystal neutron diffraction at 15 K by scanning along the c^* direction to show the presence of magnetic reflection associated with two close but different propagation wave vectors q_1 and q_2. Solid lines are fits to the peaks with two Gaussian functions along with a background term. (b) Thermal variation of the integrated intensities of various magnetic reflections obtained from NPD. Here, solid lines have been used as a guide to the eye.

FIG. 8. Magnetic and electric phase diagram of $NdMn_2O_5$ powder. Here, PM, ICM, CM, PE, and FE are abbreviated forms used to denote paramagnetic, incommensurate magnetic, commensurate magnetic, paraelectric, and ferroelectric states, respectively. The magnetic wave vectors (q_1, q_2, and q_{CM}) corresponding to each magnetic phase have been mentioned in parentheses.

not unusual in this series of compounds. Indeed, for $DyMn_2O_5$, such behavior has been reported previously [23]. It can be attributed to the presence of several quasidegenerate magnetic states due to the underlying magnetic frustration in the system. The fact that the two propagation wave vectors merge at low temperature is a lock-in effect and it reflects that the system finally stabilizes in the most favorable magnetic structure.

By further cooling below 15 K, some more new reflections emerge in the diffractograms. They are found to be associated with the same magnetic propagation wave vector. As a consequence, they seem to be connected with a spin reorientation effect, rather than to a new magnetic transition. The magnetic phase in the region of 5 K ($\sim T_{4P}$) $\leqslant T \leqslant$ 15 K (T_{3P}) can be described with only one incommensurate magnetic propagation vector q_2, and it will be denoted as the ICM2 phase afterwards.

Finally, below T_{4P}, one unique additional reflection appears and coexists with the previous ones (CM+ICM2 phase). This
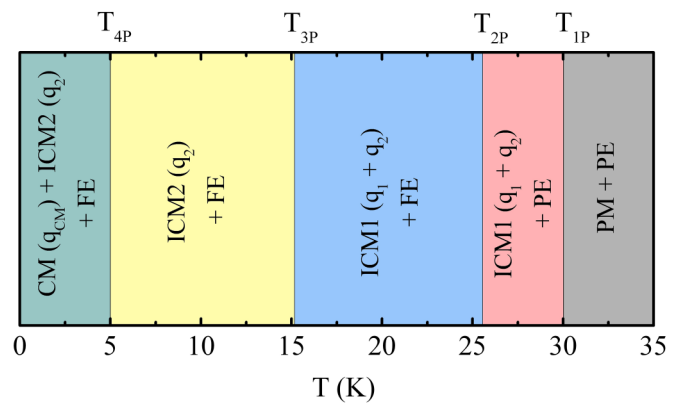
new reflection can be indexed with a commensurate $q_{CM} =$ (0.5,0,0) propagation wave vector (CM). The appearance of an additional magnetic order at low temperature is very common in this series of compounds. It is generally attributed to the ordering of the rare-earth spins following the same propagation wave vector as that of the Mn spins. The unusual feature in the present case is that the propagation wave vector associated with the rare-earth ordering is different than the one associated with the Mn spins. However, such a behavior is present in $DyMn_2O_5$ and $PrMn_2O_5$ compositions as well [13,23]. Particularly in $DyMn_2O_5$, one can observe exactly the same AF q_{CM} propagation wave vector (0.5,0,0) below 8 K, which is associated with the ordering of Dy^{3+} spin [31]. The magnetic and electric phase diagrams of the $NdMn_2O_5$ powder have been depicted in Fig. 8 for the sake of clarity.

The thermal evolution of the integrated intensities corresponding to different reflections associated with the incommensurate q_1 propagation wave vector is represented in Fig. 7(b). This parameter is proportional to the square of the magnetic order parameter. We can observe different types of behaviors based upon the nature of the (h,k,l) indices of the reflections. For the first set of reflections (reflections at $(\pm 0.5, 1, 0.4 - \delta)$ and $[\pm 0.5, 1, 2 - (0.4 - \delta)]$), the intensity increases monotonically when the system is cooled below T_{1P}. The second set of reflections (for example, $[\pm 0.5, 0, 1 - (0.4 - \delta)]$) starts to appear around $T_{3P} \pm 2$ K. There is a third set of reflections [example: $(1.5, 1, \sim 0.4)$] that emerges in between T_{1P} and T_{2P}. Unfortunately, due to the scattered nature of these reflections around this region, it is difficult to precisely determine their onset temperature. Within the error bars, no anomaly can be detected near the T_{4P} transition.

E. Determination of the magnetic structure in the ICM2 phase

For $NdMn_2O_5$, determination of the magnetic structure from the NPD data is very complicated owing to the following facts: (i) weak magnetic reflections often overlapping with the nuclear contributions, (ii) the incommensurate nature of the
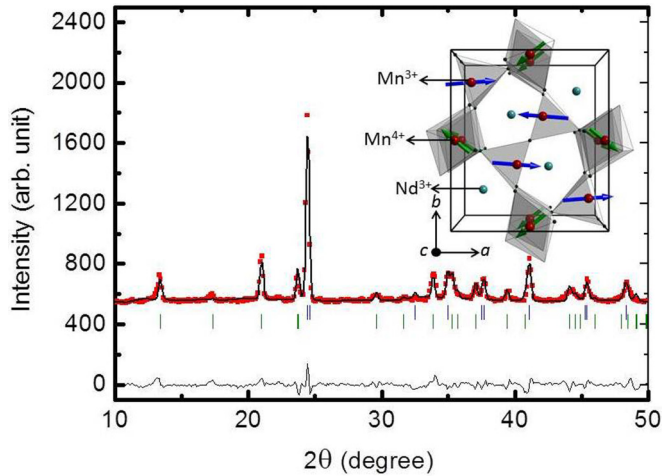
FIG. 9. (a) Rietveld refinement (experimental data: red squares; calculated profile: black solid line; allowed nuclear reflections: blue vertical marks; allowed magnetic reflections: green vertical marks) of the NPD data recorded at 15 K in the ICM2 phase. The difference between the experimental and the calculated profiles is depicted at the bottom of the graph. The inset depicts the magnetic structure as obtained from the refinement of the NPD data.

propagation wave vector, (iii) the coexistence of two slightly dissimilar propagation wave vectors q_1 and q_2, and (iv) the presence of eight $3d$ magnetic ions (four from each type) distributed in two different magnetic sublattices (Mn^{4+} and Mn^{3+}) and the four R^{3+} ions whose contributions in the successive magnetic orderings cannot be easily established.

In order to avoid the complexity related to the multiple q phase, we chose to study the magnetic structure in the ICM2 phase at 15 K. Also at this temperature the magnetic ordering only concerns the Mn spins. To reduce the number of free parameters, we carried out a symmetry analysis using the BASIRREPS program included in the FULLPROF suite package. We also imposed several constraints on the magnetic structure refinement of $NdMn_2O_5$ based on some general features of the RMn_2O_5 family and physical arguments. These constraints are as follows: (i) The magnitude of the moments for the identical ions were set to be equal. (ii) We followed a spin density wave (SDW) description of the Mn spins which seems to be physically more acceptable in this family than any kind of spiral configuration due to spin anisotropy. Such a SDW structure has also been found in many other members of this family. (iii) Magnetic moments should mainly lie in the (a,b) plane, as previously proposed for many other RMn_2O_5 compositions [31]. The last constraint is also consistent with our magnetization measurements on the platelike crystal, which clearly indicated the (a,b) plane as the easy plane.

The symmetry analysis of the RMn_2O_5 compounds of the $Pbam$ space group with a magnetic propagation vector $(\frac{1}{2},0,k_z)$ was described in detail in Ref. [31]. It has been shown that the $k_z \neq 0$ symmetry analysis does little to reduce the number of independent variables in the problem, since the positions of Mn^{4+} cation are split into two orbits, which considerably decreases the symmetry constraints. It was noted as well that a "toy model" [31] using Shubnikov formalism with exact magnetic space group symmetry $P_{2a}b'2_1m'$ can be

TABLE II. Rietveld refinement results for the magnetic structure of the powder and the single-crystal sample in the ICM2 phase at 15 and 10 K, respectively. A spherical description has been used to describe the components of the moment at the (x,y,z) positions. For the powder refinement, magnetic R_{Bragg} agreement factor $= 14.07\%$ and $q_2 = (0.5,0,0.399)$. For the single-crystal refinement, magnetic R_F factor $= 15.36\%$.

Powder: Atom	$M\ (\mu_B)$	ϕ°	θ°	Phase (2π)
Mn^{3+}				
(0.4099,0.3528,0.5)	3.53(4)	356(5)	90	0
(0.5901,0.6472,0.5)	3.53(4)	176(5)	90	0
(0.0901,0.8528,0.5)	3.53(4)	4(5)	90	0
(0.9099,0.1472,0.5)	3.53(4)	4(5)	90	0
Mn^{4+}				
(0,0.5,0.2567)	2.51(9)	145(10)	90	$-0.08(1)$
(0,0.5,0.7433)	2.51(9)	145(10)	90	0.08(1)
(0.5,0,0.2567)	2.51(9)	215(10)	90	$-0.08(1)$
(0.5,0,0.7433)	2.51(9)	215(10)	90	0.08(1)
Crystal: Atom	$M\ (\mu_B)$	ϕ°	θ°	Phase (2π)
Mn^{3+}				
(0.4114,0.3505,0.5)	3.52(6)	350(4)	90	0
(0.5886,0.6495,0.5)	3.52(6)	170(4)	90	0
(0.0886,0.8505,0.5)	3.52(6)	10(4)	90	0
(0.9114,0.1495,0.5)	3.52(6)	10(4)	90	0
Mn^{4+}				
(0,0.5,0.2557)	2.67(7)	135(9)	90	$-0.07(2)$
(0,0.5,0.7443)	2.67(7)	135(9)	90	0.07(2)
(0.5,0,0.2557)	2.67(7)	225(9)	90	$-0.07(2)$
(0.5,0,0.7443)	2.67(7)	225(9)	90	0.07(2)

used in this case to reduce the number of free parameters. We have found that, in spite of its oversimplification, the "toy model" with exact magnetic space group symmetry $P_{2a}b'2_1m'$, compatible with the predicted space group for the ferroelectric phases $Pb2_1m$, allows one to fit both our powder and single-crystal data.

Using the "toy model," we performed several refinements starting from a random spin configuration resulting in the same magnetic structure after convergence. The difference between the experimental and the calculated NPD intensities (magnetic $R_{Bragg} = 14.5\%$), as obtained from the refinement, is depicted in Fig. 9. As seen from Table II and the inset of Fig. 9, Mn^{3+} spins lie close to the a direction and carry a moment of $3.50\mu_B$, whereas Mn^{4+} carries a smaller moment ($2.67\mu_B$) lying in the ab plane. The fact that the Mn^{3+} spins are nearly parallel to the a axis is in agreement with our single-crystal magnetization data showing a weak AF-like behavior near 26 K only for the field applied in the a direction. Starting from the spin configuration above, we attempted to improve the fit by relaxing the constraints of the "toy model" and replacing them by various FM (or AFM) coupling constraints of the Mn moment by pairs. However, no significant improvement of the agreement factor was found in these cases.

To validate the magnetic structure determined from the NPD data at 15 K, we performed a single-crystal neutron diffraction experiment. This measurement was carried out with

a wavelength of 2.345 Å on the $6T_2$ diffractometer [32] at the Orphée-LLB reactor (France). Due to the very small size of the platelike crystal (<0.2 mm^3) only a limited number of magnetic reflections was observed. However, nearly 40 magnetic reflections with intensities greater than 3σ were recorded at 10 K. With the help of the FULLPROF software, we carried out a rigorous refinement following the step by step methodology used to refine the NPD data and achieved a R_F factor of 15.4% for the magnetic structure. We found that the magnetic structure as obtained after the final refinement is extremely close to that obtained from the NPD data (Table II).

IV. DISCUSSION AND CONCLUSION

To understand the characteristics of the magnetic states in NdMn$_2$O$_5$ is an intricate issue. Concerning the nature of the propagation wave vectors in the entire temperature range, it can be observed that at least one of the components remains incommensurate. Another important point is that the c^* components of the propagation vectors q_1 and q_2 are close to 0.5, the value observed in Pr, La, and Bi based RMn$_2$O$_5$ compositions [12,33]. Such a c^* component indicates that the exchange interaction J_1 between two Mn^{4+} spins through the Nd^{3+} layer is AF-like. It probably originates from the fact that the Mn^{4+}-Nd^{3+}-Mn^{4+} exchange path is weak and thus the main contribution to J_1 comes from the AF Mn^{4+}-Mn^{4+} superexchange interaction through a shared oxygen. This result is supporting a strong R^{3+} size effect controlling the magnetic phase diagram of the RMn$_2$O$_5$ series [13,34].

Regarding the magnetic structure at 15 K, Mn^{3+} spins are found to lie nearly along the a direction. This feature is similar to some other RMn$_2$O$_5$ ($R =$ Tb, Ho, Y) members, as found earlier. Another interesting aspect in the magnetic structure of NdMn$_2$O$_5$ is the relatively large noncollinearity between the Mn^{3+} and Mn^{4+} sublattices in contrast to the other multiferroic members of this family. However, compared to the structure of PrMn$_2$O$_5$, where these two sublattices are nearly orthogonal, the noncollinearity is much less in NdMn$_2$O$_5$ ($\sim$30°). The degree of such noncollinearity could be connected with the strength of the underlying magnetic frustration that varies with the composition. It is interesting to notice that the Nd ions are not involved in the magnetic ordering at 15 K, unlike the scenario observed in TbMn$_2$O$_5$ and HoMn$_2$O$_5$ where the Tb and Ho spins are partially ordered even at 27 and 26 K, respectively [31].

Concerning the multiferroic properties, our work unveils that NdMn$_2$O$_5$ is ferroelectric with a weak electric polarization of maximum $\sim$2.5 μC/m^2 (about ten times smaller than the one measured in TbMn$_2$O$_5$), which also changes its sign at low temperatures. Such a small P value indicates that the magnetoelectric coupling, responsible for the emergence of the electric polarization, is very small in the present case. On the other hand, the sign reversal of P is presumably related to the thermal evolution of the magnetic structure. This kind of magnetic structure dependence on the polarization is not very uncommon in this series. In TbMn$_2$O$_5$, it has been observed that a sufficiently strong magnetic field can drastically modify the magnetic structure, which in effect results in the reversal of the polarization [3]. We also show in this series of compounds that the emergence and the existence of the FE transition is not associated with the commensurate character of the propagation wave vector. This result also supports the fact that the commensurate character is not mandatory for the stabilization of the ferroelectricity. However, the very small magnitude of polarization could be related either to the incommensurate nature of the magnetic propagation vector or to the noncollinearity of the spins involved in the exchange-striction effect since the polarization is proportional to the scalar product of the adjacent spins.

In conclusion, our study shows that NdMn$_2$O$_5$ is multiferroic, although its magnetic and electric properties differ from the other multiferroic RMn$_2$O$_5$ compositions with small R^{3+} size. The results establish the strong influence of rare-earth size on the magnetoelectric phase diagram [34]. The study also confirms that a threshold R^{3+} size effect is dominant in PrMn$_2$O$_5$ and NdMn$_2$O$_5$ [13]. Our investigation thus paves the way for further theoretical works to understand the strong R^{3+} size effect in the multiferroic properties of this series.

[1] W. Eerenstein, N. D. Mathur, and J. F. Scott, Nature (London) **442**, 759 (2006).

[2] I. A. Sergienko and E. Dagotto, Phys. Rev. B **73**, 094434 (2006).

[3] S. W. Cheong and M. Mostovoy, Nat. Mater. **6**, 13 (2007).

[4] I. Kagomiya, K. Kohn, and T. Uchiyama, Ferroelectrics **280**, 131 (2002).

[5] J. A. Alonso, M. T. Casais, M. J. Martinez-Lope, J. L. Martinez, and M. T. Fernandez-Diaz, J. Phys.: Condens. Matter **9**, 8515 (1997).

[6] V. Balédent, S. Chattopadhyay, P. Fertey, M. B. Lepetit, M. Greenblatt, B. Wanklyn, F. O. Saouma, J. I. Jang, and P. Foury-Leylekian, Phys. Rev. Lett. **114**, 117601 (2015).

[7] M. B. Lepetit (private communication).

[8] P. G. Radaelli and L. C. Chapon, J. Phys.: Condens. Matter **20**, 434213 (2008).

[9] L. C. Chapon, G. R. Blake, M. J. Gutmann, S. Park, N. Hur, P. G. Radaelli, and S.-W. Cheong, Phys. Rev. Lett. **93**, 177402 (2004).

[10] S. Petit, V. Balédent, C. Doubrovsky, M. B. Lepetit, M. Greenblatt, B. Wanklyn, and P. Foury-Leylekian, Phys. Rev. B **87**, 140301(R) (2013).

[11] N. Hur, S. Park, P. A. Sharma, J. S. Ahn, S. Guha, and S.-W. Cheong, Nature (London) **429**, 392 (2004).

[12] C. Doubrovsky, G. Andre, F. Bouquet, E. Elkaim, M. Li, M. Greenblatt, and P. Foury-Leylekian, Physica B **407**, 1718 (2012).

[13] C. Doubrovsky, G. Andre, A. Gukasov, P. Auban-Senzier, C. R. Pasquier, E. Elkaim, M. Li, M. Greenblatt, F. Damay, and P. Foury-Leylekian, Phys. Rev. B **86**, 174417 (2012).

[14] G. Buisson, Phys. Status Solidi **16**, 533 (1973); **17**, 191 (1973).

[15] I. A. Zobkalo, S. V. Gavrilov, N. Z. Saw Nyi, S. N. Barilo, and S. V. Shiryaev, J. Magn. Magn. Mater. **354**, 85 (2014).

[16] S. Chattopadhyay, V. Baledent, P. Auban-Senzier, C. Pasquier, C. Doubrovsky, M. Greenblatt, and P. Foury-Leylekian, Physica B **460**, 214 (2015).

[17] G. Popov, M. Greenblatt, and W. H. McCarroll, Mater. Res. Bull. **35**, 1661 (2000).

[18] P. Euzen, P. Leone, C. Gueho, and P. Palvadeau, Acta Crystallogr. Sect. C **49**, 1875 (1993).

[19] A. C. Larson and R. B. Von Dreele, Los Alamos National Laboratory Report No. LAUR 86-748, 2001 (unpublished).

[20] G. M. Sheldrick, in *Computational Crystallography*, edited by D. Sayre (Clarendon, Oxford, U.K., 1982), pp. 506–514.

[21] M. Tachibana, K. Akiyama, H. Kawaji, and T. Atake, Phys. Rev. B **72**, 224425 (2005).

[22] A. P. Ramirez, Czech. J. Phys. **46**, 3247 (1996).

[23] W. Ratcliff, V. Kiryukhin, M. Kenzelmann, S.-H. Lee, R. Erwin, J. Schefer, N. Hur, S. Park, and S.-W. Cheong, Phys. Rev. B **72**, 060407(R) (2005).

[24] S. Chattopadhyay, S. Giri, and S. Majumdar, Phys. Status Solidi B **250**, 1913 (2013).

[25] Y. Jo, K.-H. Jang, J.-G. Park, H. C. Kim, T. H. Kim, K. H. Kim, N. Hur, S. Park, and S.-W. Cheong, Phys. Rev. B **76**, 012406 (2007).

[26] Z. Y. Zhao, M. F. Liu, X. Li, L. Lin, Z. B. Yan, S. Dong, and J.-M. Liu, Sci. Rep. **4**, 3984 (2014).

[27] J. Rodriguez-Carvajal, Physica B **192**, 55 (1993).

[28] C. Wilkinson, P. J. Brown, and T. Chatterji, Phys. Rev. B **84**, 224422 (2011).

[29] Y. Noda, H. Kimura, M. Fukunaga, S. Kobayashi, I. Kagomiya, and K. Kohn, J. Phys.: Condens. Matter **20**, 434206 (2008).

[30] J. Koo, C. Song, S. Ji, J.-S. Lee, J. Park, T.-H. Jang, C.-H. Yang, J.-H. Park, Y. H. Jeong, K.-B. Lee, T. Y. Koo, Y. J. Park, J.-Y. Kim, D. Wermeille, A. I. Goldman, G. Srajer, S. Park, and S.-W. Cheong, Phys. Rev. Lett. **99**, 197601 (2007).

[31] G. R. Blake, L. C. Chapon, P. G. Radaelli, S. Park, N. Hur, S.-W. Cheong, and J. Rodriguez-Carvajal, Phys. Rev. B **71**, 214402 (2005).

[32] A. Gukasov, A. Goujon, J. L. Meuriot, C. Person, G. Exil, and G. Koskas, Physica B **397**, 131 (2007).

[33] A. Munoz, J. A. Alonso, M. T. Casais, M. J. Martinez-Lope, J. L. Martinez, and M. T. Fernandez-Diaz, Eur. J. Inorg. Chem. **2005**, 685 (2005).

[34] C. Ma, J. Q. Yan, K. W. Dennis, R. W. McCallum, and X. Tan, J. Solid State Chem. **182**, 3013 (2009).